Analytical expression of long-exposure adaptive-optics-corrected coronagraphic image. First application to exoplanet detection

J.-F. Sauvage,[1,3,*] L. M. Mugnier,[1,3] G. Rousset,[2,3] and T. Fusco[1,3]

[1]*Office National d'Etudes et de Recherches Aérospatiales, Département d'optique théorique et appliquée, 29 avenue de la division Leclerc, F-92322 Châtillon, France*

[2]*Laboratoire d'Etude et d'Instrumentation en Astrophysique, Observatoire de Paris, 5 place J. Janssen 92195 Meudon Cedex, France*

[3]*Groupement d'intérêt scientifique PHASE (Partenariat Haute résolution angulaire Sol Espace) among ONERA, Observatoire de Paris, CNRS, and université Diderot*

[*]*Corresponding author: jean-francois.sauvage@onera.fr*

Received February 18, 2010; revised July 16, 2010; accepted August 9, 2010; posted August 23, 2010 (Doc. ID 124445); published September 20, 2010

In this paper we derive an analytical model of a long-exposure star image for an adaptive-optics(AO)-corrected coronagraphic imaging system. This expression accounts for static aberrations upstream and downstream of the coronagraphic mask as well as turbulence residuals. It is based on the perfect coronagraph model. The analytical model is validated by means of simulations using the design and parameters of the SPHERE instrument. The analytical model is also compared to a simulated four-quadrant phase-mask coronagraph. Then, its sensitivity to a miscalibration of structure function and upstream static aberrations is studied, and the impact on exoplanet detectability is quantified. Last, a first inversion method is presented for a simulation case using a single monochromatic image with no reference. The obtained result shows a planet detectability increase by two orders of magnitude with respect to the raw image. This analytical model presents numerous potential applications in coronographic imaging, such as exoplanet direct detection, and circumstellar disk observation.

OCIS codes: 070.0070, 110.0115.

1. INTRODUCTION

The direct imaging of exoplanets is a challenging goal of today's astronomy. For instance, the photons emitted by exoplanets carry information about the chemical composition of the planet's atmosphere and may indicate the possibility of life on it. Nevertheless, the fact that planets are often very close and very faint with respect to their parent star makes their observation very difficult. This kind of observation therefore requires the combination of extreme AO (XAO) systems, coronagraphic devices, and sophisticated dedicated postprocessing methods [1,2]. The XAO system allows a highly efficient correction of the wavefront induced by atmospheric turbulence. This correction performs a concentration of both star and planet photons and helps disentangling one from the other. The coronagraphic stage allows the rejection of most of the star signal and its associated photon noise. But still, the combined use of these two devices is not sufficient. The signal of the planet often remains hidden in the residual photons coming from the star. A postprocessing method must be derived in order to detect the planet in this residual image. If the image formation model is convolutive, the image formation is fully described by the instrument's long-exposure point-spread function (PSF). In the case of an AO system without coronagraph, imaging within the isoplanatic patch is given by a convolution and the long-exposure PSF is well described by the residual phase structure function and by the static aberrations.

The computation of long-exposure AO-corrected PSFs with neither a coronagraph nor static aberrations is a well-known issue addressed in several publications. First, [3,4] studied PSF formation with averaged realistic AO residuals. The residual structure function D_φ was introduced, as well as the notion of stationarity. Later, [5–7] provided fundamental bases for the understanding of the intimate structure of high-Streh-ratio instantaneous PSFs without a coronagraph. In particular, this work revealed the central symmetry properties of high-Strehl-ratio PSF speckle structures. The work presented in these papers relies on a Taylor expansion of the PSF to the first order for Bloemhoff, second order for Sivaramakrishnan, and nth order for Perrin, relying on the hypothesis of small aberrations. More recently, [8] developed the expression for the first-order coronagraphic PSF, but without the long-exposure expression. We strive in this paper to develop an expression with coronagraph, without the small amplitude phase approximation, and that is valid for a long exposure, thus for ground-based imaging. An often appropriate way to process images is then deconvolution. But coronagraphic imaging is precisely not a convolutive process, as it induces a non-uniform transmission in the focal plane. Conventional deconvolution is therefore not possible. Moreover, no parametric model of long-exposure coronagraphic image formation is currently available. Failing such a model, the methods currently used to process coronagraphic images may be classified

into two kinds. The first one consists in the numerical removal of the residual star signal after coronagraphy by differential imaging methods. This removal is done by performing an angular [9–11] and/or spectral [12,13] image subtraction. The subtraction needs at least two images, which leads to an increase of noise in the combined image. This method is sensitive to the temporal evolution of aberrations, or to the differential aberrations between spectral channels. The second kind consists in the estimation of both planet and star responses [14]. In this second approach, the star estimation is non-parametric, i.e., it is simply given by its pixel response in the whole field, which means several tens of thousands of coefficients. The latter coefficients are not useful for planet detection, and are thus so-called nuisance parameters for the problem at hand. In contrast, the planet, which is the only quantity of interest, is parameterized by its position and flux, i.e., three coefficients. This is clearly suboptimal from a statistical standpoint. We strive here to propose an analytical expression of the long-exposure response of the instrument for a point-like source. Such an expression will allow one to subtract the star signal numerically, therefore with neither image subtraction nor non-parameteric star response estimation. In Section2, the image formation is studied. The analytical expression is obtained for the short-exposure and the long-exposure cases. This section introduces the notion of perfect coronagraph. In Section 3, our analytical model is validated by a comparison to numerical simulations with a perfect coronagraph, and with a four-quadrant phase mask coronagraph (FQPM). In Section 4, the case of a deconvolution-like algorithm is studied: a coronagraphic image is restored by making use of the star image model.

2. ANALYTICAL CORONAGRAPHIC STAR IMAGE MODEL

In this section we derive the analytical short- and long-exposure coronagraphic image model of a point-like source. Because this model will be mostly useful for computing the star image, we shall focus on an on-axis point-source in the following. However, the following developments are valid whatever the point position may be. The model for a coronagraphic point source image will be called "coronagraphic PSF", which is of course field-dependent.

A. Model Hypothesis

We introduce here the notations and formalism of the whole paper, as well as the assumptions. The main optical items are gathered on Fig. 1: the system components, the optical aberrations, the turbulence residuals, and the coronagraphic device.

The optical system is composed of a telescope, a coronagraph, and a detector plane. The telescope pupil plane is indexed by 0. The coronagraph mask plane is indexed by 1, with notation $-$ and $+$ for before and after the coronagraphic mask. The pupil plane after the coronagraph is indexed by 2, with notation $-$ and $+$ for before and after the Lyot stop. The detector plane is indexed by 3. The analytical response of this system is obtained by assuming a propagation of the electromagnetic wave from the telescope to the detector plane described by the Fraunhofer diffraction, i.e., by a Fourier transform between successive planes. The field amplitudes in the pupil planes are denoted $\Psi_0(\rho)$ and $\Psi_2(\rho)$, with ρ the pupil spatial variable. The field amplitudes in the focal plane are denoted $\mathcal{A}_1(\alpha)$ and $\mathcal{A}_3(\alpha)$, with α the focal plane spatial variable, i.e., an angle on the sky.

The aberrations in the system are separated into two main contributions: the time-dependent ones, and the static ones. All aberrations are assumed to be introduced in a pupil plane, i.e., no Fresnel effect is considered here.

Time-dependent aberrations are due to atmospheric turbulence. They are AO-corrected, and the residual aberrations are denoted $\varphi_r(\rho,t)$. We consider $\varphi_r(\rho,t)$ as a time-dependent random phase in the entrance pupil plane. It is assumed Gaussian centered, stationary (in particular, its phase variance is uniform on the pupil), and ergodic with respect to time. φ_r is generated in the telescope pupil plane.

Static aberrations are introduced by optical defects or misalignments. Among the static aberrations, we distinguish aberrations introduced upstream and downstream of the coronagraphic mask. We denote the first ones by $\varphi_u(\rho)$, and the latter ones by $\varphi_d(\rho)$. We assume that these

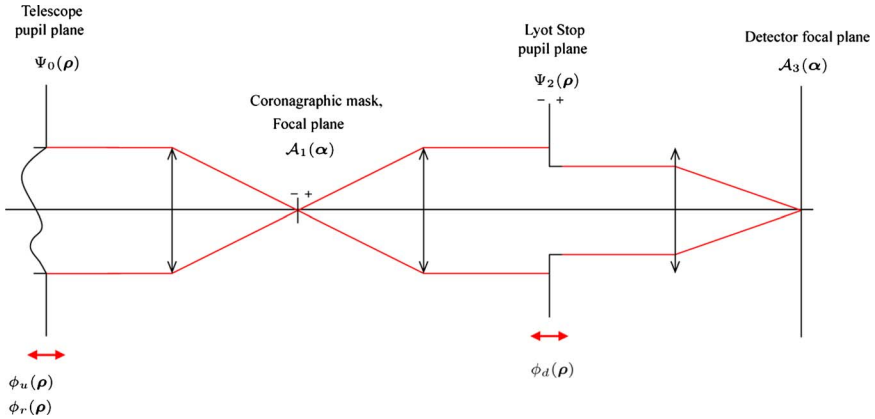

Fig. 1. (Color online) Optical scheme of a coronagraphic imager. The upstream and downstream static aberrations as well as the adopted notations are φ_u and φ_d respectively. $\mathcal{A}_i(\alpha)$ denote focal plane complex amplitudes, while $\Psi_i(\rho)$ denote pupil plane amplitudes.

aberrations are introduced in a pupil plane: φ_u is introduced in the telescope pupil plane 0, and φ_d is introduced in the Lyot plane 2.

Moreover, the upstream aberration φ_u may include a tip–tilt component to account for the star position w.r.t. the optical axis, and in particular for a possible static misalignment between the star and the coronagraph. The model for an off-axis point source can be derived by adding the corresponding tip–tilt in the static aberrations.

We define here the perfect coronagraph model through its action on the incoming light wave. The notion of a perfect coronagraph has already been introduced by [8,15,16]. The perfect coronagraph is always defined as an optical device that subtracts a centered Airy pattern from the electromagnetic field. This subtraction may be analytically expressed either in pupil or focal plane. Only the weight of the subtracted Airy pattern, denoted by η in the following, differs from one definition to another. The connection between our definition of the perfect coronagraph and that adopted in [15,8] is given in Appendix A.

The perfect coronagraph subtracts an Airy pattern from the complex amplitude of the incoming field wave in a proportion that minimizes the energy coming out from the coronagraphic mask. We will introduce the corresponding formalism in Subsection 2.B. As the perfect coronagraph does not have a real focal plane extension, there is no need for a Lyot stop in principle. Nevertheless, the downstream pupil is taken into account in the following for comparison with the FQPM coronagraph.

B. Short-Exposure Analytical Model

We begin in this section by describing the complex amplitudes in all planes of interest for a short exposure. The goal of this first model is to describe the instantaneous distribution of light in the detector focal plane. The complex amplitude in the entrance pupil plane is given by

$$\Psi_0(\boldsymbol{\rho},t) = \mathcal{P}_u(\boldsymbol{\rho})e^{j(\varphi_r(\boldsymbol{\rho},t)+\varphi_u(\boldsymbol{\rho}))}, \tag{1}$$

where $\mathcal{P}_u(\rho)$ is the telescope pupil function.

The amplitude $\mathcal{A}_1^-$ immediately before the coronagraphic mask is given by the inverse Fourier transform (FT) of the previous amplitude,

$$\mathcal{A}_1^-(\boldsymbol{\alpha},t) = \mathrm{FT}^{-1}(\Psi_0(\boldsymbol{\rho},t)) = \mathrm{FT}^{-1}(\mathcal{P}_u(\boldsymbol{\rho})e^{j(\varphi_r(\boldsymbol{\rho},t)+\varphi_u(\boldsymbol{\rho}))}), \tag{2}$$

where the inverse FT between the focal plane $\mathcal{A}_1^-(\alpha,t)$ and the pupil plane $\Psi_0(\rho,t)$ is defined by the relation

$$\mathcal{A}_1^-(\boldsymbol{\alpha},t) = \int_{-\infty}^{+\infty}\int_{-\infty}^{+\infty}\Psi_0(\boldsymbol{\rho},t)e^{-2j\pi\boldsymbol{\alpha}\boldsymbol{\rho}}\mathrm{d}^2\boldsymbol{\rho}. \tag{3}$$

We choose the convention of inverse FT for describing wave propagation from pupil to focal plane, and FT for the converse. This choice simplifies forthcoming equations as it allows the object to conserve its orientation in all focal planes. It is nothing else than an arbitrary orientation of axes in focal planes. As introduced in Subsection 2.A, the action of the perfect coronagraph is to minimize the energy coming out from the coronagraphic mask by subtracting an Airy pattern's amplitude $\mathrm{FT}^{-1}(\mathcal{P}_u(\rho))$. If we denote by η the weight of an Airy pattern's amplitude subtracted from the incoming wave, the corresponding focal plane amplitude $\mathcal{A}_1^+(\alpha,t)$ is then given by relation

$$\mathcal{A}_1^+(\boldsymbol{\alpha},t) = \mathcal{A}_1^-(\boldsymbol{\alpha},t) - \eta(t)\mathrm{FT}^{-1}(\mathcal{P}_u(\boldsymbol{\rho})). \tag{4}$$

We denote by η_0 the optimal value of η that minimizes the outcoming energy:

$$\eta_0(t) = \arg\min_{\eta(t)}\|\mathcal{A}_1^-(\boldsymbol{\alpha},t) - \eta(t)\mathrm{FT}^{-1}(\mathcal{P}_u(\boldsymbol{\rho}))\|^2, \tag{5}$$

and we define the perfect coronagraph by Eq. (4) with $\eta(t)=\eta_0(t)$ given by Eq. (5).

The solution $\eta_0(t)$ of this least-squares minimization is well known: it corresponds to the projection of the incoming field $\mathcal{A}_1^-$ on the Airy pattern. Using Parseval's theorem, this can be written in a pupil plane:

$$\eta_0(t) = \langle\Psi_0(\boldsymbol{\rho},t)|\mathcal{P}_u(\boldsymbol{\rho})\rangle, \tag{6}$$

where $\langle|\rangle$ is the usual scalar product defined on functions f and g of a 2D variable ρ:

$$\langle f|g\rangle = \frac{1}{S}\int\int_S f^*(\boldsymbol{\rho})g(\boldsymbol{\rho})\mathrm{d}^2\boldsymbol{\rho}.$$

$|\eta_0(t)|^2$ is therefore the exact definition of the instantaneous Strehl ratio as defined by Born and Wolf [17]. For an off-axis source, the Strehl ratio tends rapidly to zero. The wave subtracted by the perfect coronagraph therefore also tends to zero, which means that the outcoming wave after the coronagraph $\mathcal{A}_1^+$ tends toward $\mathcal{A}_1^-$: the farther the source is from the optical axis, the smaller the action of the coronagraph. The so-defined perfect coronagraph accounts for the aberrations introduced upstream of the coronagraphic mask. The weight of the subtracted Airy pattern (η) accounts for the total amount of aberrations upstream of the mask. An example of tilted PSF is shown on Fig. 2, where we can see the shape of coronagraphic PSF for a perfect coronagraph for different values of tip–tilt upstream aberration from −1.6 to 1.6 rad.

We will keep in the following a circular uniform pupil, but this simplified model of coronagraphic mask may easily account for a non-uniform pupil shape, as with central obstruction, apodization, or spider arms. Our goal in this paper is not to demonstrate a high extinction rate for a realistic optical system, as many publications before did it very well. Our goal is to demonstrate that our formalism is able to describe simply the imaging by a realistic long-exposure coronagraphic system.

Fig. 2. (Color online) Coronagraph response for a system comprising pure tip–tilt from −1.6 to 1.6 rad. Central PSF is completely obscured as the perfect coronagraph presents an infinite extinction for a non-aberrant system.

The amplitude $\Psi_2^-(\rho,t)$ just before pupil plane 2 is given by the FT of $\mathcal{A}_1^+(\alpha,t)$:

$$\Psi_2^-(\boldsymbol{\rho},t) = \mathrm{FT}(\mathcal{A}_1^+(\boldsymbol{\alpha},t)) = e^{j(\varphi_r(\boldsymbol{\rho},t)+\varphi_u(\boldsymbol{\rho}))}\mathcal{P}_u(\boldsymbol{\rho}) - \eta_0(t)\mathcal{P}_u(\boldsymbol{\rho}). \tag{7}$$

Plane 2 introduces the action of the Lyot stop and of the static aberrations downstream of the Lyot stop. For the sake of conciseness, we shall omit the spatial variables ρ and α in the following, in order to alleviate reading. The only remaining explicit variable is the time t. The amplitude $\psi_2^+(t)$ just after pupil plane 2 is then

$$\Psi_2^+(t) = \Psi_2^-(t)\mathcal{P}_d e^{j\varphi_d} = \mathcal{P}_d e^{j(\varphi_r(t)+\varphi_u+\varphi_d)} - \eta_0(t)\mathcal{P}_d e^{j\varphi_d}, \tag{8}$$

with $\mathcal{P}_d$ the pupil function of the Lyot stop and φ_d the aberrations downstream of the coronagraph. As the diameter of $\mathcal{P}_d$ is usually taken smaller than the diameter of $\mathcal{P}_u$, the product $\mathcal{P}_u\mathcal{P}_d$ has been replaced by $\mathcal{P}_d$ in Eq. (8). The focal plane amplitude in the detector plane is then finally given by the inverse FT of Ψ_2^+:

$$\mathcal{A}_3(t) = \mathrm{FT}^{-1}(\Psi_2^+(t)) = \mathcal{A}_n(t) - \eta_0(t)\mathcal{A}_d, \tag{9}$$

with

$$\mathcal{A}_n(t) = \mathrm{FT}^{-1}(\mathcal{P}_d e^{j(\varphi_r(t)+\varphi_u+\varphi_d)}),$$

$$\mathcal{A}_d = \mathrm{FT}^{-1}(\mathcal{P}_d e^{j\varphi_d}), \tag{10}$$

with $\mathcal{A}_n$ the focal plane amplitude without coronagraphic mask but with the Lyot stop and all the aberrations, and $\mathcal{A}_d$ the focal plane amplitude due to the sole static aberrations downstream of the coronagraph.

For the perfect coronagraph, and in the trivial case where $\varphi_r=\varphi_u=0$, we obtain $\eta_0=1$ even if $\varphi_d\neq 0$ by means of Eqs. (1) and (6), so the outgoing intensity is null. This is consistent with the fact, well known by coronagraphic system designers, that upstream aberrations are much more critical than downstream ones for system performance.

The instantaneous intensity distribution h_3 in the detector plane is given by the square modulus of $\mathcal{A}_3$:

$$h_3(t) = \mathcal{A}_3(t)\mathcal{A}_3^\star(t) = |\mathcal{A}_n(t) - \eta_0(t)\mathcal{A}_d|^2 = \mathcal{A}_n(t)\mathcal{A}_n^\star(t) + |\eta_0(t)|^2\mathcal{A}_d\mathcal{A}_d^\star - 2\Re(\eta_0^\star(t)\mathcal{A}_n(t)\mathcal{A}_d^\star). \tag{11}$$

The expression of $h_3(t)$ comprises the cross product of focal plane amplitudes $\mathcal{A}_n(t)$ and $\mathcal{A}_d^\star$. With this expression, the action of the coronagraph can clearly be interpreted as creating a wave in "phase opposition" w.r.t. $\mathcal{A}_n$, and the resulting intensity in the focal plane is the interference figure between these two waves. In Eq. (11), the purely static term is $\mathcal{A}_d^\star$. All the other terms depend on the AO-corrected wave front $\varphi_r(t)$.

C. Long-Exposure Analytical Model

We now compute the long-exposure coronagraphic star image h_c. It is given by the expected value of the short exposure $\langle h_3(t)\rangle$. In practice, this will be given by a time average of short exposures $h_3(t)$. The aim of this computation is to express it as a function of statistical parameters such as the structure function D_{φ_r} and pupil aberrations φ_u and φ_d:

$$h_c = \langle h_3(t)\rangle = h_n + \langle|\eta_0(t)|^2\rangle\mathcal{A}_d\mathcal{A}_d^\star - 2\Re(\langle\eta_0(t)\mathcal{A}_n^\star(t)\rangle\mathcal{A}_d), \tag{12}$$

with

$$h_n \triangleq \langle\mathcal{A}_n(t)\mathcal{A}_n^\star(t)\rangle. \tag{13}$$

The two first terms of Eq. (12) are easily identified. The first term, h_n, is the long-exposure PSF without coronagraph but using the Lyot stop. This PSF can be written as the convolution of two terms, static OTF and turbulent OTF, which can be written in Fourier space as

$$\tilde{h}_n = (\mathcal{P}_d e^{j(\varphi_u+\varphi_d)} \otimes \mathcal{P}_d e^{j(\varphi_u+\varphi_d)}) \cdot e^{-1/2D_{\varphi_r}}, \tag{14}$$

assuming in the remainder of the paper that the residual phase is stationary [18]. The second term of Eq. (12), $\langle|\eta_0(t)|^2\rangle\mathcal{A}_d\mathcal{A}_d^\star$, is the mean PSF obtained with the sole downstream aberrations, weighted by the mean Strehl ratio during observation. The term $\langle|\eta_0(t)|^2\rangle$ can be rewritten as a function of the study parameters:

$$\begin{aligned}\langle|\eta_0(t)|^2\rangle &= \frac{1}{S^2}\int\int \mathcal{P}_u(\boldsymbol{\rho})\mathcal{P}_u(\boldsymbol{\rho}') \times \langle e^{(j(\varphi_r(\boldsymbol{\rho},t)+\varphi_u(\boldsymbol{\rho}))-j(\varphi_r(\boldsymbol{\rho}',t)+\varphi_u(\boldsymbol{\rho}')))}\rangle \mathrm{d}\boldsymbol{\rho}\mathrm{d}\boldsymbol{\rho}' \\ &= \frac{1}{S^2}\int\int \mathcal{P}_u(\boldsymbol{\rho})\mathcal{P}_u(\boldsymbol{\rho}')e^{-1/2D_{\varphi_r}(\boldsymbol{\rho}'-\boldsymbol{\rho})+j(\varphi_u(\boldsymbol{\rho})-\varphi_u(\boldsymbol{\rho}'))} \times \mathrm{d}\boldsymbol{\rho}\mathrm{d}\boldsymbol{\rho}', \end{aligned} \tag{15}$$

$$= \frac{1}{S^2}\int\int (e^{-1/2D_\varphi}\star\Psi_u)(\boldsymbol{\rho}')\cdot\Psi_u^\star(\boldsymbol{\rho}')\mathrm{d}\boldsymbol{\rho}', \tag{16}$$

with $D_{\varphi_r}(\rho'-\rho)$ the residual phase structure function and Ψ_u the static field in the pupil corresponding to static upstream aberrations φ_u:

$$\Psi_u = \mathcal{P}_u e^{j\varphi_u}. \tag{17}$$

Assuming the stationarity of φ_r, the coefficient $\langle|\eta_0(t)|^2\rangle$ therefore depends only on statistical and deterministic parameters, namely the residual phase structure function and the upstream aberrations.

We now turn to the third term of Eq. (12), in order to express it as a function of statistical quantities. In order to obtain a useful expression for the term $\langle\eta_0^\star(t)\mathcal{A}_n(t)\rangle$, it is mandatory to expand the two quantities η_0 and $\mathcal{A}_n$. The first one is the average of the incoming field on the pupil, the second one is the FT of the field without coronagraph on pupil $\mathcal{P}_d$:

$$\langle\eta_0^\star(t)\mathcal{A}_n(\boldsymbol{\alpha},t)\rangle = \frac{1}{S}\left\langle\int\int_{\boldsymbol{\rho}}\mathcal{P}_u(\boldsymbol{\rho})e^{-j(\varphi_u(\boldsymbol{\rho})+\varphi_r(\boldsymbol{\rho},t))} \times \int\int_{\boldsymbol{\rho}'}\mathcal{P}_d(\boldsymbol{\rho}')e^{j(\varphi_r(\boldsymbol{\rho}',t)+\varphi_u(\boldsymbol{\rho}')+\varphi_d(\boldsymbol{\rho}'))} \times e^{-2j\pi\boldsymbol{\alpha}\boldsymbol{\rho}'}\mathrm{d}\boldsymbol{\rho}\mathrm{d}\boldsymbol{\rho}'\right\rangle. \tag{18}$$

Grouping the integrals together and leaving the deterministic quantities outside of the expected value yields

$$\langle \eta_0^\star(t)\mathcal{A}_n(\boldsymbol{\alpha},t)\rangle = \frac{1}{S}\int\int\int\int_{\boldsymbol{\rho},\boldsymbol{\rho}'} \langle e^{j(\varphi_r(\boldsymbol{\rho}',t)-\varphi_r(\boldsymbol{\rho},t))}\rangle \times \mathcal{P}_u(\boldsymbol{\rho})\mathcal{P}_d(\boldsymbol{\rho}')e^{-j\varphi_u(\boldsymbol{\rho})}e^{j(\varphi_u(\boldsymbol{\rho}')+\varphi_d(\boldsymbol{\rho}'))} \times e^{-2j\pi\boldsymbol{\alpha}\boldsymbol{\rho}'}\mathrm{d}\boldsymbol{\rho}\mathrm{d}\boldsymbol{\rho}'. \quad (19)$$

The structure function of the residual phase is easily identified as the first factor in this integral. Additionally under the assumed stationarity of $\varphi_r(t)$, the structure function does not depend on ρ and ρ' but only on the difference $\rho'-\rho$ and is written $D_{\varphi_r}(\rho'-\rho)$ [3,4]:

$$\langle \eta_0^\star(t)\mathcal{A}_n(\boldsymbol{\alpha},t)\rangle = \frac{1}{S}\int\int\int\int_{\boldsymbol{\rho},\boldsymbol{\rho}'} e^{-1/2D_{\varphi_r}(\boldsymbol{\rho}'-\boldsymbol{\rho})}\mathcal{P}_u(\boldsymbol{\rho})\mathcal{P}_d(\boldsymbol{\rho}') \times e^{-j\varphi_u(\boldsymbol{\rho})}e^{j(\varphi_u(\boldsymbol{\rho}')+\varphi_d(\boldsymbol{\rho}'))}e^{-2j\pi\boldsymbol{\alpha}\boldsymbol{\rho}'}\mathrm{d}\boldsymbol{\rho}\mathrm{d}\boldsymbol{\rho}'. \quad (20)$$

We now gather all the terms depending on ρ under the same integral; the convolution product $\star$ of the residual turbulent OTF with amplitude $\Psi_u^\star(\alpha)$ therefore appears:

$$\langle \eta_0^\star(t)\mathcal{A}_n(\boldsymbol{\alpha},t)\rangle = \frac{1}{S}\int\int_{\boldsymbol{\rho}'} \mathcal{P}_d(\boldsymbol{\rho}')e^{j(\varphi_u(\boldsymbol{\rho}')+\varphi_d(\boldsymbol{\rho}'))} \times \underbrace{\left[\int\int_{\boldsymbol{\rho}} e^{-1/2D_{\varphi_r}(\boldsymbol{\rho}'-\boldsymbol{\rho})}\mathcal{P}_u(\boldsymbol{\rho})e^{-j\varphi_u(\boldsymbol{\rho})}\mathrm{d}\boldsymbol{\rho}\right]}_{(e^{-1/2D_{\varphi_r}}\star\Psi_u^\star)(\boldsymbol{\rho}')} e^{-2j\pi\boldsymbol{\alpha}\boldsymbol{\rho}'}\mathrm{d}\boldsymbol{\rho}'. \quad (21)$$

It is now possible to express the term $\langle \eta_0^\star(t)\mathcal{A}_n(\alpha,t)\rangle$ with respect to deterministic quantities such as the residual phase structure function and the static aberrations:

$$\langle \eta_0^\star(t)\mathcal{A}_n(\boldsymbol{\alpha},t)\rangle = \frac{1}{S}\mathrm{FT}^{-1}[\Psi_{ud}(\boldsymbol{\rho})\cdot(e^{-1/2D_\varphi}\star\Psi_u^\star)(\boldsymbol{\rho})], \quad (22)$$

with

$$\Psi_{ud}(\boldsymbol{\rho}) = \mathcal{P}_d(\boldsymbol{\rho})e^{j(\varphi_u(\boldsymbol{\rho})+\varphi_d(\boldsymbol{\rho}))}. \quad (23)$$

Combining this last result with Eq. (12) finally yields the following expression for the coronagraphic long-exposure on-axis star image:

$$h_c = h_n + \langle|\eta_0(t)|^2\rangle h_d - \frac{2}{S}\Re\{\mathrm{FT}^{-1}[\Psi_{ud}\times(e^{-1/2D_{\varphi_r}}\star\Psi_u^\star)]\mathcal{A}_d^\star\}. \quad (24)$$

This expression gives the long-exposure light distribution of the star observed with a perfect coronagraph. This expression takes into account upstream and downstream aberrations, as well as residual turbulence and a Lyot stop. This long-exposure description is the key point of the coronagraphic imaging. To the best of our knowledge, this is the first time that such an expression is obtained with so few assumptions. We validate this model in Section 3. This direct model for coronagraphic observation should improve exoplanet detection, as it allows one to develop dedicated coronagraphic image inversion methods, an example of which is given in Section 4.

3. VALIDATION OF THE ANALYTICAL MODEL BY SIMULATIONS

We validate in this section the analytical long-exposure coronagraphic image model. The numerical simulation conditions are given in Subsection 3.A. In Subsection 3.B we compare our analytical model to a simulated one. The simulation is performed by summing a large number of short-exposure simulated images of an on-axis point source. In Subsection 3.C, we compare our analytical response of a perfect coronagraph to that of a real coronagraph, namely a FQPM coronagraph. We investigate in Subsections 3.D and 3.E the sensitivity of the proposed analytical model to an imperfect calibration of the observing parameters to be used in the computation of the analytic model.

A. Validation Conditions

We consider here point-like stars and companions observed with a ground-based 8 m telescope equipped with AO. The simulations take into account both the AO-corrected turbulence and static aberrations. The baseline AO system considered is the high-performance AO system SAXO [19] of the SPHERE instrument [2]. We use a Fourier-based simulation method that describes the AO via the spatial power spectrum of the residual phase [20] and is presented in [19]. The power spectral density (PSD) of the residual phase after AO correction has already been used to design the SPHERE instrument [19]. The AO residual PSD includes servo-lag term, fitting term, RON and photon noise, and spatially-filtered Shack–Hartmann [21,22]. The simulation takes the following realistic set of parameters: a 41×41 subaperture Shack–Hartmann, a 1.2 kHz sampling frequency, a guide star of magnitude 8, a Kolmogorov turbulence, and a seeing of 0.8 arcsec at 0.5 μm. It is to be noted that the pupil considered in the following simulations is circular and without any central obstruction. Such a pupil is certainly too simple and unrealistic w.r.t. a real telescope system, but our goal here is to validate an image formation model with a simple system. Moreover we know that the efficiency of the coronagraph will decrease with a real pupil (i.e., with central occultation). In addition to the turbulence residuals, we need to define a typical set of static aberrations in our simulations. Following the analysis performed for the specification of the SPHERE instrument, we consider a spatial spectrum of upstream aberrations

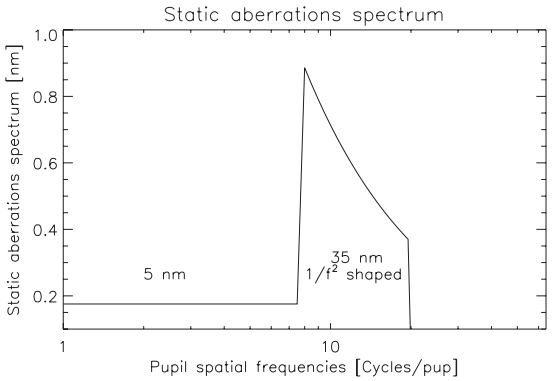

Fig. 3. Static aberrations spectrum upstream of the coronagraph mask. Low frequencies are assumed to be precompensated down to a residual of 5 mm. The medium frequencies follow a $1/f^2$ shaped spectrum, with an RMS value of 35 nm. The total RMS value of the OPD of the upstream aberrations is $\sigma_u = 35.3$ nm.

that follows the shape shown in Fig. 3. The low frequencies (up to 8 cycles per pupil) are assumed to be compensated down to a residual wavefront error of 5 nm through a careful calibration, *e.g.*, by phase diversity [23]. The medium frequencies from 8 to 20 cycles per pupil (the AO cut-off frequency) present a total standard deviation of 35 nm. The total RMS optical path difference (OPD) error of the upstream wavefront is thus $\sigma_u = 35.3$ nm. No spatial frequency for static aberrations above 20 cycles per pupil is considered here. Of course this choice is unrealistic as we know that realistic systems present some aberrations at those spatial frequencies. But the impact of static aberrations is negligible compared to residual turbulence outside the AO halo. Moreover, the choice of f^{-2} is rather pessimistic, as the M_1 mirror of the Very Large Telescope (VLT) presents a f^{-3} PSD (real measurement). Downstream static aberrations are randomly generated according to a f^{-2} spectrum, f being the spatial frequency in the pupil, with a total RMS OPD error of 100 nm. Images are computed at a wavelength $\lambda = 1.6$ μm and are Shannon-sampled. The static aberrations are assumed to be calibrated, but not compensated. The SPHERE instrument is planned to combine images obtained simultaneously at different wavelengths on different imaging paths. Even if the AO loop could compensate for static aberrations on one path, differential static aberrations would be present on the other path, and calibrated.

In Fig. 4, we present the typical profiles of long-exposure star images with and without coronagraph for the conditions considered in this paper. The circularly averaged intensity profiles are plotted with respect to field of view, and the intensity is normalized to the incoming total intensity in the entrance pupil. In other words, the integral of h_n (Eq. (13), PSF without coronagraph) is 1. The value of h_n at the origin of Fig. 4 is thus proportional to the Strehl ratio. The proportionality factor is 0.14 if the PSF is centered between 4 pixels and 0.20 if the PSF is centered on one pixel. The focal plane area located between 0 and $20\lambda/D$ is the PSF area cleaned by the AO correction, while the area beyond $20\lambda/D$ is corrugated by the residual halo due to the uncorrected high spatial frequencies of the turbulence. Here $SR = 87\%$. We observe the huge gain brought by the coronagraph for angular separations lower than $20\lambda/D$. We also plot the level of the maximum intensity of a planet of contrast 2.10^4. This level depends on how the planet is centered w.r.t. the pixel grid. The two horizontal dashed–dotted lines represent the best and worst cases (planet at center of pixel and between 4 pixels, respectively). The upstream aberration-induced speckles are the principal contributor to the star residual between 8 and $20\lambda/D$. The AO residuals are dominant below $8\lambda/D$ and beyond $20\lambda/D$. With a wavefront error of 35 nm, it is not possible (or only marginally) to detect a planet of contrast 2.10^4 between 0 and $20\lambda/D$ from a single image.

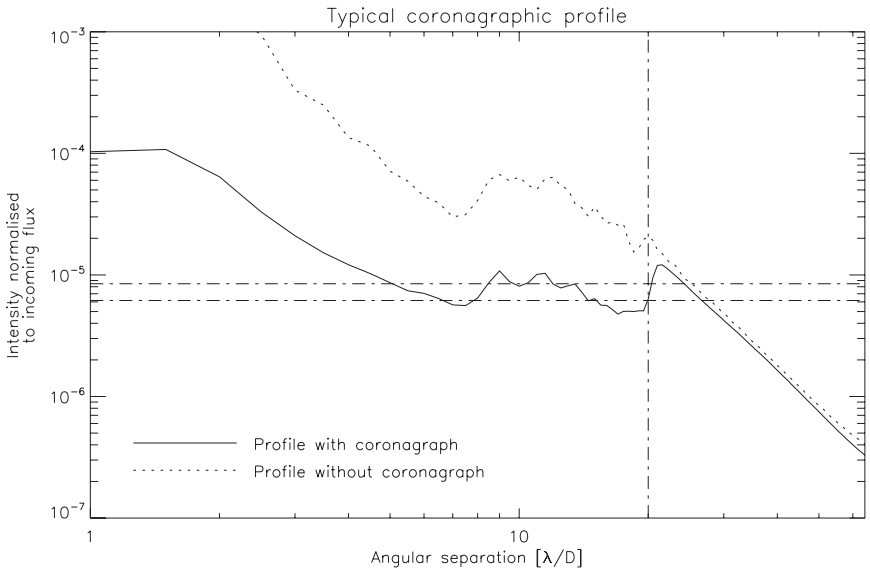

Fig. 4. Profiles of long-exposure star images with and without coronagraph for the conditions given in Subsection , including AO residuals (SPHERE case), upstream and downstream aberrations, perfect coronagraph, at wavelength $\lambda = 1.6$ μm. Profiles normalized to 1 photon in the entrance pupil. Horizontal dotted–dashed lines: maximum intensity for a planet of contrast 2.10^4 (centered on 1 pixel and between 4 pixels). Vertical dotted–dashed line: cutoff of the AO correction ($20\lambda/D$).

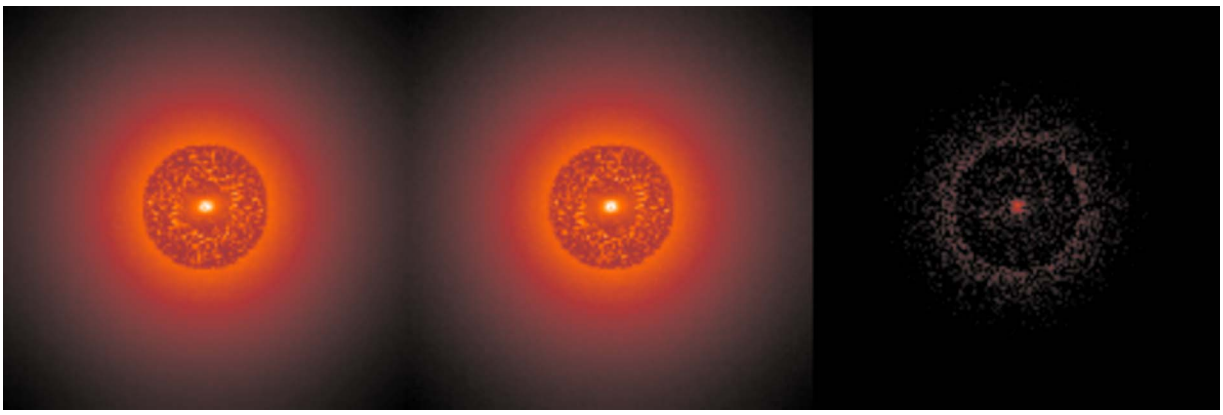

Fig. 5. (Color online) (Left) Analytical model, (center) simulated coronagraphic PSF with $N=1000$ turbulence realizations, and (right) absolute value of difference in log-scale and same dynamic. The image formation includes residual turbulence and static aberrations. The conditions of simulation are the ones explained in Subsection 3.A.

B. Long-Exposure Analytical Model versus Sum of Short-Exposure Images

The validation of the long-exposure image model has been performed by comparing Eq. (24) for h_c with an empirical long-exposure PSF. The latter is obtained by summing N short-exposure coronagraphic PSF's $h_3(\varphi_{r,k})$. Each short-exposure coronagraphic PSF is numerically simulated with an independent realization of a residual turbulence phase screen $\varphi_{r,k}$ following the Fourier approach, the addition of the upstream aberrations—the propagation of the light field by Fourier transform taking into account the stops and masks presented in Fig. 1—a perfect coronagraph, and the downstream aberrations, as explained in Subsection 2.B [Eq. (11)]. The expression for the empirical long-exposure PSF is therefore

$$\langle h_3\rangle_N = \frac{1}{N}\sum_{k=1}^{N} h_3(\varphi_{r,k}). \tag{25}$$

In order to compare PSF generated with different conditions, we introduce here the notion of circularly averaged error profile. This profile is defined as follows:

$$\varepsilon(\alpha) = \sqrt{\frac{1}{2\pi}\int_0^{2\pi} (h_c(\alpha,\theta) - \langle h_3\rangle_N(\alpha,\theta))^2 \mathrm{d}\theta}, \tag{26}$$

with (α,θ) the polar coordinate variables, h_c being by instance the coronagraphic PSF computed analytically, and $\langle h_3\rangle_N$ being the simulated one, with summation of N short exposures. This error term is relevant to compare the shape of two PSFs with respect to angular separation. This does give only a very rough idea of detectability reachable with the model, as it shows the average RMS residual after subtracting the model image from the simulated one.

The results of Fig. 5 show the numerical empirical and analytical coronagraphic images of a centered star and the error term as defined previously in log-scale and the same dynamic range. The analytical model shows a very good matching of the global structure of the response: the residuals are mostly situated on the most luminous part (AO halo and on-axis residual). These residuals are mainly due to the finite exposure time of the empirical long exposure. We plot in Fig. 6 the circularly averaged

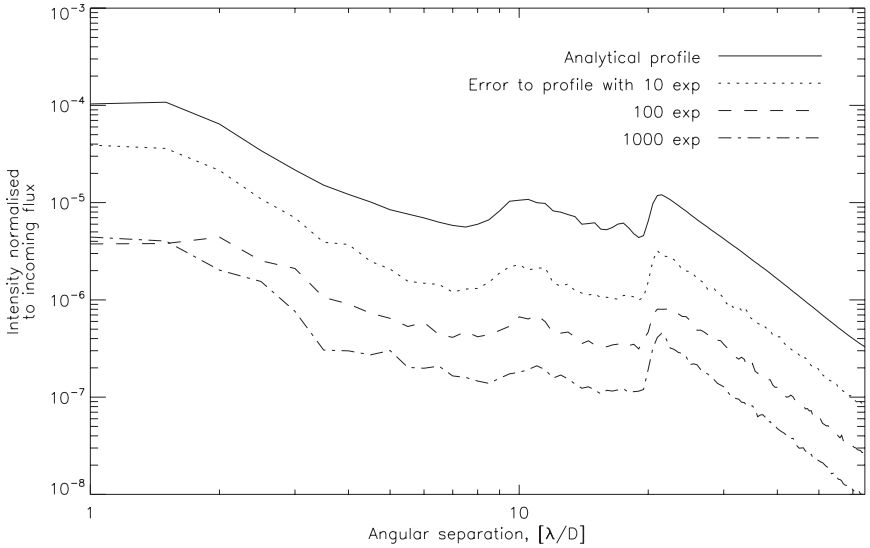

Fig. 6. Circularly averaged profiles of error between the analytical model and the simulated star image. The profiles are plotted for different cases of long-exposure convergence. The image formation includes residual turbulence and static aberrations. The simulation conditions are explained in Subsection 3.A.

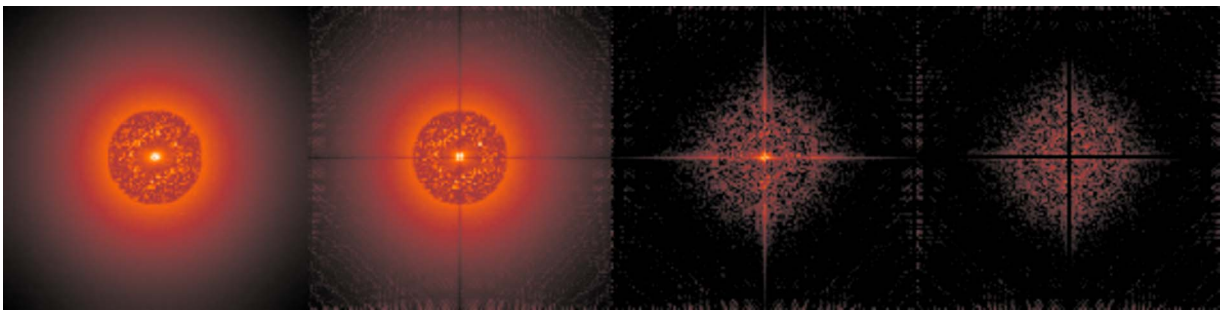

Fig. 7. (Color online) (Left) Analytical model , (center left) FQPM coronagraphic PSF simulated, (center right) absolute value of difference, and (right) the same without accounting for the biquadrants points (log-scale, same dynamic). The image formation includes residual turbulence and static aberrations. The conditions of simulation are the ones explained in Subsection 3.A.

analytical intensity profile and error profiles for the empirical long-exposure PSF. The profiles are normalized by the total number of photons in the entrance pupil. We observe, as expected, that the error decreases as the number of short-exposure images increases, with a decrease by a factor $\sqrt{10}$ for an increase of the number of short exposures by a factor of 10. A summation of 1000 independent short exposures corresponds to a typical observing time of 10 to 100 s, which is realistic. These simulation results validate the model, which describes correctly the structure of the long-exposure coronagraphic PSF for a perfect coronagraph.

C. Perfect Coronagraph Model versus FQPM Coronagraph

One of the coronagraphs that will be implemented on SPHERE is a FQPM [24]. This coronagraph is based on the principle of an original mask design, a four-quadrant binary phase mask. The mutually destructive interferences of the coherent light from the main source produce a very efficient nulling, which is theoretically able to completely cancel the incoming light in the case of a monochromatic, perfectly manufactured mask, an aberration-free wave, and in the absence of a central obstruction in the telescope.

In order to validate our long-exposure analytical model with respect to more realistic coronagraphs, we have compared it to the empirical long-exposure coronagraphic image obtained with a FQPM coronagraph. For this simulation, the perfect coronagraph has been replaced by a FPQM. Figure 7 shows the on-axis star response of such a coronagraph compared to our analytical model. Except for the field positions situated on the X and Y axes, the difference between the two coronagraphic images is very small at any position. Figure 8 shows the error profile between the analytical model and the simulated FQPM coronagraph after removal of points around the X and Y axes. The relative difference ranges between 3% and 8% for any field position $\alpha > 2\lambda/D$ and is only slightly larger than the convergence error of Fig. 6 for 1000 exposures. Therefore, our model, although derived for a perfect coronagraph, is appropriate to process data obtained with a FQPM coronagraph.

D. Miscalibration of the Structure Function

We first study the influence of a miscalibration of the structure function D_{φ_r}. The test performed by simulation is as follows:

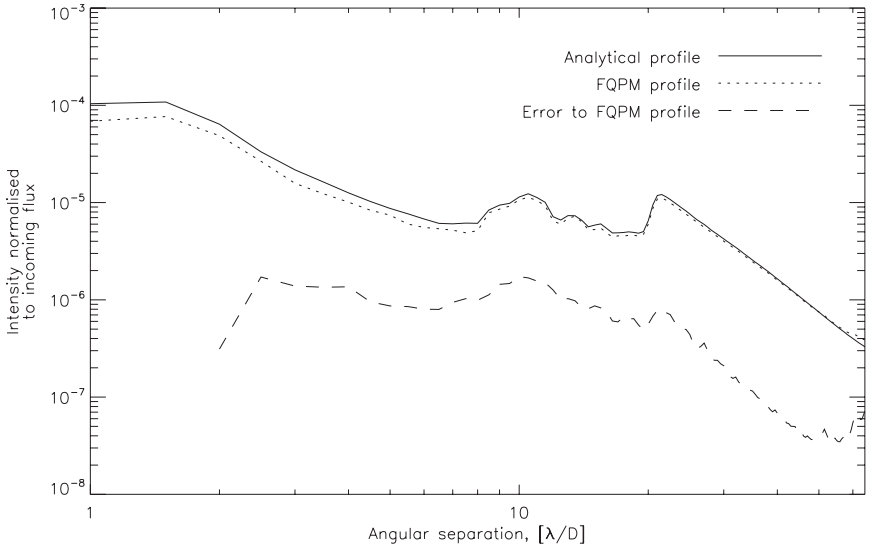

Fig. 8. Circularly averaged profiles of error between the analytical model and the simulated star image with FPQM coronagraph. The image formation includes residual turbulence and static aberrations. The simulation conditions are explained in Subsection 3.A.

- computation of long-exposure coronagraphic star image h_c using our model with the true D_{φ_r} (conditions given in Subsection 3.A);
- computation of long exposure coronagraphic star image $\hat{h}_c$ using our model but with miscalibrated D_{φ_r}, denoted $\hat{D}_\varphi$, where

$$\hat{D}_\varphi = \beta D_{\varphi_r},$$

with β=0.8 to 0.95, corresponding for instance to a poor estimation of the seeing conditions. This is a rough way to introduce miscalibration, as a modification of turbulence conditions would result in more complexity;

- computation of the differential image $h_\Delta = h_c - \hat{h}_c$.

We present in Fig. 9 the impact of the miscalibration of D_{φ_r} on the differential image h_Δ. Circularly averaged profiles are plotted for β=0.8, 0.9, and 0.95. The profile of h_c is also plotted as reference. For β=0.9, subtracting $\hat{h}_c$ instead of h_c from an image would still bring a substantial attenuation of the residual star light, typically a factor of the order of 10. This shows that such an error in the calibration of D_{φ_r} will not dramatically jeopardize the detection of planets of contrast lower than 10^5. But to achieve higher contrast, the requirement on the quality of the calibration is more stringent.

E. Miscalibration of the Upstream Static Aberrations

Second, we study the influence of the miscalibration of the static aberrations. Concerning the downstream static aberrations, we found a negligible impact of their miscalibration on the image difference. Indeed, these aberrations have a very weak contribution to the image formation in a coronagraphic instrument, as already pointed out in [8]. The only aberrations studied herein are the ones introduced upstream of the coronagraphic mask, φ_u. The test performed by simulation is as follows:

- computation of long-exposure coronagraphic star image h_c using our model with the true φ_u (conditions given in Subsection 3.A);
- computation of long-exposure coronagraphic star image $\hat{h}_c$ using our model but with miscalibrated φ_u, denoted $\hat{\varphi}$, where

$$\hat{\varphi} = (1+\varepsilon)\cdot\varphi_u,$$

with ε chosen positive or negative in a way that the error on φ_u ranges from 0.00 to 0.20;

- computation of the differential image $h_\Delta = h_c - \hat{h}_c$.

We compute the profiles of the differential images h_Δ for different RMS wavefront errors for $\hat{\varphi}$: ε=0.05 to 0.30. In Fig. 10, the profiles are plotted with respect to angular separation. The major impact of the miscalibration of the upstream aberrations is inside the AO halo. A calibration error of the order of 10 nm (ε=0.20) for $\hat{\varphi}$ with respect to φ_u significantly limits the detectability of a planet between 8 and 20λ/D, which corresponds to the spatial frequency range of the dominant upstream aberrations of our simulations. To obtain an attenuation of a factor 10 of the residual star light after subtraction, the error between $\hat{\varphi}$ and φ_u must be smaller than or equal to 3.5 nm (ε=0.10). This is a demanding requirement for the calibration of φ_u, but it seems achievable with optimized and accurate techniques [23]. It allows one to detect planets of contrast 2.10^4. To detect at higher contrasts requires reducing the amplitude of the upstream aberrations, using several wavelengths (spectral differential imaging or integral field spectrographs), and/or using field rotation to disentangle speckles from planets [9,11].

An effectiveness comparison can be done here for the computation of coronagraphic PSF. On the one hand, our model is costless in term of numerical computation, compared to the simulation of 1000 empirical PSFs. Moreover, the computation given by our model is exact, and does not suffer from convergence errors. On the other

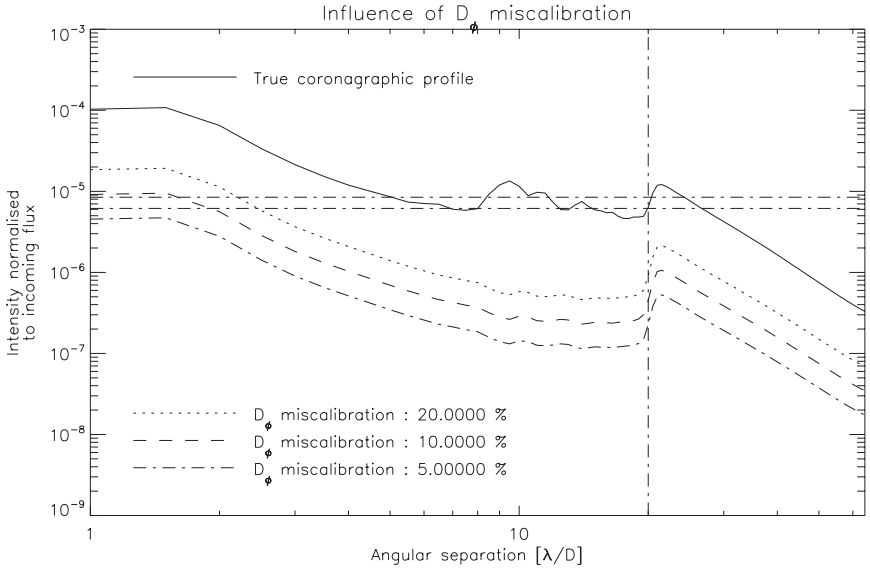

Fig. 9. Profiles of the difference h_Δ for different error levels on the miscalibration of the structure function. Dotted curve, β=0.8. Dashed curve, β=0.9. Dotted–dashed curve, β=0.95. Continuous curve, profile of h_c. For lines and conditions see caption of Fig. 4.

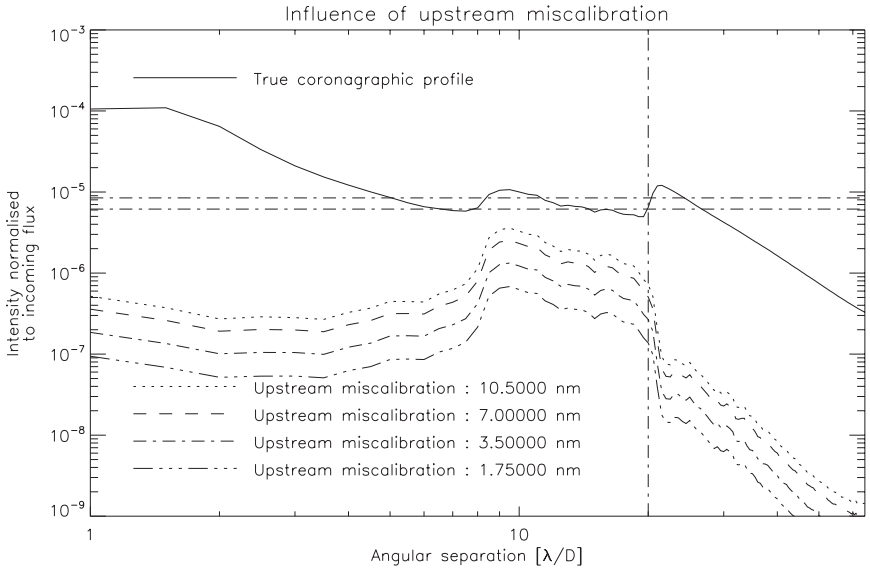

Fig. 10. Profiles of the difference h_Δ for different calibration errors of the upstream aberrations. Dotted curve, $\varepsilon=0.05$ (1.75 nm). Dashed curve, $\varepsilon=0.10$ (3.5 nm). Dotted–dashed, $\varepsilon=0.20$ (7.0 nm). Dot dot dot–dash, $\varepsilon=0.30$ (10.5 nm). Continuous curve, profile of h_c. For lines and conditions see caption of Fig. 4.

hand, the simple coronagraph model used in our PSF computation does not allow one to describe correctly the residual very close to the optical axis after a realistic coronagraph. The impact of such model errors very close to the optical axis is actually modest because planets will be searched for farther away from the axis. We will see in Section 4 another feature of a simple image formation model: this capability may be very useful in the case of an inversion model, where the observed object or the system parameters will have to be estimated.

We have seen that the subtraction of the analytical model allows one to gain in detectability. The next section will show a more optimized inversion process that in particular incorporates the estimation of the star flux.

4. TOWARD PLANET DETECTION: USE OF THE ANALYTICAL MODEL IN AN INVERSION METHOD

This analytical model has been implemented into an inversion method described below. First, we develop a simplified direct model of image formation in a coronagraphic case. Then we describe the planet estimation assuming that the upstream and downstream aberrations and the phase structure function have been calibrated prior to the deconvolution.

A. Two-PSF Model and Image Formation

The exact computation of an observed scene through a coronagraphic instrument requires knowledge of the field-dependent PSF $h(\alpha,\alpha')$ in the whole field, where α' is the position of a point source and α the current position in the image. Although we have just derived such an expression, the manipulation of such massive data may be computationally expensive. However in the framework of exoplanet detection, the observed scene is composed of one bright on-axis point-like source, the star, and a possible weak off-axis environment. In the simple case of a Lyot coronagraph, for instance, the light coming from a source at position α' away from the optical axis is only slightly affected by the focal mask: the PSF $h(\alpha,\alpha')$ away from the axis is very close to the PSF $h_n(\alpha)$ of Eq. (13) without a coronagraphic mask. Close to the optical axis, on the contrary, the structure of the PSF is strongly perturbated by the presence of the coronagraphic mask. The study of Malbet [25] shows that the PSF may be approximated by $h_n(\alpha)$ outside a small transition zone λ/D wide around the focal mask. For the perfect coronagraph

$$h(\boldsymbol{\alpha},\boldsymbol{\alpha}') \simeq h_n(\boldsymbol{\alpha}-\boldsymbol{\alpha}') \text{ for } |\boldsymbol{\alpha}'| > \lambda/D. \tag{27}$$

Therefore a simplified model of the image formation is chosen in the following and accounts for two PSF's: one on-axis h_c for the star following the model developed in Section 2 and one off-axis h_n without coronagraphic mask for the faint environment. This approach is valid for any off-axis environment, be it an extended scene or one or more point-like sources.

As a consequence, we will decompose the astrophysical target into two parts: the star itself, whose light is partially rejected by the coronagraph, and its environment, called hereafter the object and denoted by $o(\alpha)$, which is the object of interest, the observed scene without the star signal. Let us denote by $\mathbf{i}$ the recorded, discrete image, where the boldface recalls that it is a vector concatenating all pixels. Similarly, let us denote by $\mathbf{o}$, $\mathbf{h_c}$, $\mathbf{h_n}$ the discretized versions of functions $o(\alpha)$, $h_c(\alpha)$, $h_n(\alpha)$. The image formation of the star and its environment may then be rewritten as

$$\mathbf{i} = F_0 \cdot \mathbf{h_c} + \mathbf{h_n} \star \mathbf{o}, \tag{28}$$

where F_0 stands for the star flux in the pupil before the coronagraph and $\star$ for the convolution product. We consider that the object is a 2D map of intensity $\mathbf{o}$ to be estimated and not a set of Dirac functions whose amplitude and position are unknown. We recall that $\mathbf{h_c}$ can be computed from Eq. (24) based on the calibrations of the structure function of the turbulent phase and the upstream

and downstream pupil static aberrations. In the following, we assume that these calibrations are available but imperfect by 5%, which means an error of 1.75 nm RMS for φ_u calibration, and an error of 11 nm on D_φ calibration. Hence, the parameters to be estimated in Eq. (28) are the object $\mathbf{o}$ and the star flux F_0.

B. Joint Estimation of Star Flux and Object

As in differential imaging [26], we would like to calibrate the residual star light $F_0\mathbf{h_c}$ and subtract it from the image in order to retrieve the star's faint environment. We propose here to jointly fit the star flux F_0 and estimate the unknown object $\mathbf{o}$. The joint estimation is done by minimizing a global MAP criterion $\mathcal{J}$ [Equation (29)] with respect to the unknowns F_0 and $\mathbf{o}$:

$$\mathcal{J}(F_0,\mathbf{o}) = \left\| \frac{(\mathbf{i} - F_0 \cdot \mathbf{h_c}) - (\mathbf{h_n} \star \mathbf{o})}{\sigma_b} \right\|^2 + \mathcal{J}_{F_0}(F_0) + \mathcal{J}_{\mathbf{o}}(\mathbf{o}), \tag{29}$$

where σ_b^2 is the noise variance (depending on pixel position), and $\mathcal{J}_{F_0}(F_0)$ and $\mathcal{J}_{\mathbf{o}}(\mathbf{o})$ are the regularization terms incorporating *a priori* knowledge of parameters to estimate.

In practice, this minimization is done by alternating the estimation of these two parameters F_0 and $\mathbf{o}$, i.e., by minimizing the criterion alternately with respect to each of the unknowns, considering that the other one is fixed. As the criterion is quadratic with F_0, the solution of the star flux for the current estimate of the object is given by the analytical expression

$$\hat{F}_0(\mathbf{o}) = \frac{\sum_{\boldsymbol{\alpha}} (\mathbf{i} - \mathbf{h_n} \star \mathbf{o}) \cdot \mathbf{h_c}(\boldsymbol{\alpha}) / \sigma_b^2(\boldsymbol{\alpha})}{\sum_{\boldsymbol{\alpha}} \mathbf{h_c}(\boldsymbol{\alpha}) / \sigma_b^2(\boldsymbol{\alpha})}. \tag{30}$$

For the first iteration, $\mathbf{o}$ is set to zero.

Then for the current estimation of F_0, minimization of Eq. (29) is equivalent to a classical minimization of the following maximum *a priori* (MAP) criterion:

$$\mathcal{J}(\mathbf{o},\hat{F}_0) = \left\| \frac{\mathbf{i}_\Delta(\hat{F}_0) - \mathbf{h_n} \star \mathbf{o}}{\sigma_b} \right\|^2 + \mathcal{J}_{\mathbf{o}}(\mathbf{o}) + \quad \textit{constant} \tag{31}$$

where the differential image $\mathbf{i}_\Delta(\hat{F}_0)$ is defined as

$$\mathbf{i}_\Delta(\hat{F}_0) = \mathbf{i} - \hat{F}_0 \cdot \mathbf{h_c}.$$

$\mathcal{J}_{\mathbf{o}}(\mathbf{o})$ is for instance a quadratic Wiener-type regularization [27] based on a parametric model of the PSD of the object. We use the MISTRAL code [28] to minimize Eq. (31) and estimate the object under the positivity constraint. As in ([29], Appendix A), all hyperparameters (noise variance and object PSD) are estimated in an unsupervised fashion prior to deconvolution by maximum likelihood. At convergence, $\mathbf{i}_\Delta$ contains our best estimate of the star-subtracted image of the object. In practice, for an object much fainter than the central star, one global iteration, i.e., one F_0 estimation followed by one $\mathbf{o}$ estimation, is enough.

In Figs. 11 and 12, we present an example of the proposed method to estimate planets in the environment of a star from a long-exposure AO-corrected coronagraphic image. The conditions are the ones given in Subsection 3.A. In the image on the left in Fig. 11, we observe the simulated empirical long-exposure coronagraphic image including photon noise, for $F_0 = 10^{10}$ photons. This flux corresponds to a $G0$-type star of H magnitude 8 and an exposure time of 100 sec with a global throughput of 13% for such an instrument [2]. The detector electronic noise is assumed to be negligible. Center image is i_Δ after subtraction of the star response at the first iteration. Here, $\mathbf{h_c}$ is computed considering imperfect calibrations of the structure function D_{φ_r} ($\beta = 0.95$) and of the upstream aberrations φ_u ($\varepsilon = 0.05$) corresponding to a RMS wavefront error of 1.75 nm compared to the true aberrations. These conditions are quite conservative in view of the capability of the techniques for turbulence and aberration calibrations to be implemented in SPHERE [23,30]. The companion of contrast 2.10^4 is barely discernible but still convolved by the PSF. The image on the right shows the result of object map $\mathbf{o}$ after deconvolution. We define the

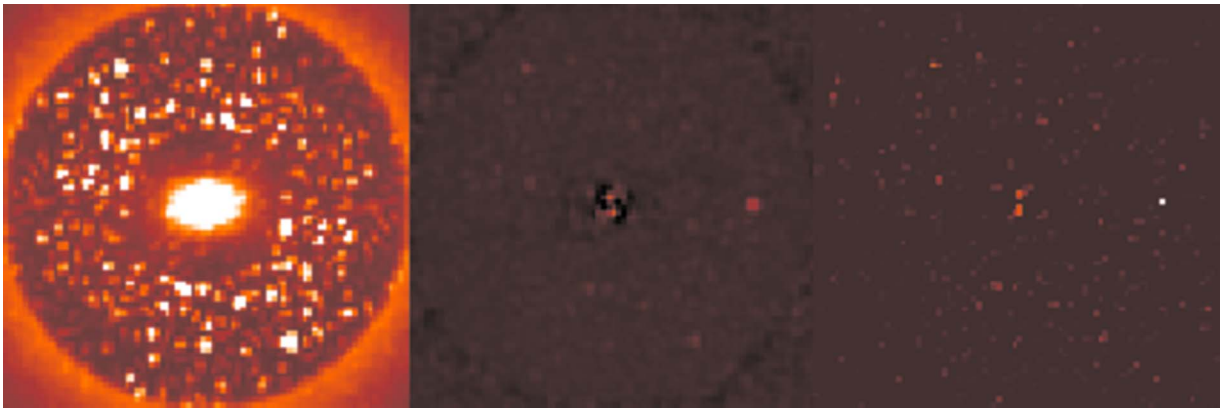

Fig. 11. (Color online) (Left) Simulated empirical long-exposure coronagraphic star image with a companion of contrast 2.10^4 and separation $14\lambda/D$, sum of 1000 short exposures, star photon flux $F_0 = 10^{10}$, perfect coronagraph; (center) differential image i_Δ of the star environment after subtraction of the star response $\hat{F}_0 \cdot \mathbf{h_c}$ computed with miscalibrated D_{φ_r} ($\beta = 0.95$) and φ_u ($\varepsilon = 0.05$); (right) object map after MAP deconvolution. Images are in linear scale, the star residual is saturated, only the AO-corrected area is shown, up to $20\lambda/D$. For the detailed simulation conditions see Subsection 3.A.

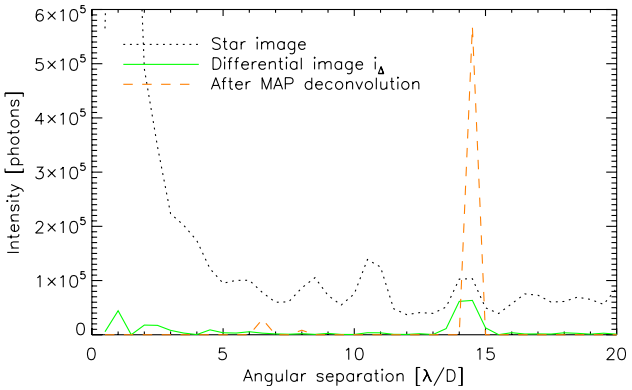

Fig. 12. (Color online) Horizontal profile of Fig. 11, linear scale.

SNR of the companion as the ratio of the estimated maximum flux of the companion in the considered plane (raw image, difference image, and deconvolved object) over the RMS value of background signal taken in a crown situated at the expected companion's radius. The maximum flux of the companion is estimated as the maximum measured intensity around the expected companion position, minus the average value of intensity estimated in the same crown.

In the raw image (left), the companion's SNR is estimated to be slightly less than 1. In the difference image (center), the SNR is of the order of 25. In the object 2D map after MAP deconvolution (right), the SNR is more than 100, which is a significant enhancement. The gain is a factor of more than 4, as expected, corresponding roughly to the mean number of pixels in the core of the PSF. The gain compared to the raw image is of two orders of magnitude. We have shown here a simple inversion method using the coronagraphic image formation model. This method uses the coronagraphic image formation model in order to estimate the star flux and the observed object, assuming the system parameters are quite well known. In the more realistic case where the system parameters are unknown, or miscalibrated, this model should be of prime help for developing a focal-plane coronagraphic wave-front sensor or a structure function estimator [31]. This kind of estimation requires the use of a criterion minimization, which implies the computation of the image formation model typically a few hundreds, which can definitely not be done with a summation of 1000 empirical PSFs. Of course the estimation of more parameters than star flux and the object intensity requires additional information. This additional information is given by more images differing by a known diversity, as an introduced calibrated aberration, or images recorded at several wavelengths. A more sophisticated algorithm has therefore to be developed, able to deal with numerous images and to estimate the aberrations as well as the residual structure function and the observed object. For instance, this model will be of prime help in dealing with the hyperspectral image cubes that will be acquired on SPHERE Integral Field Spectrograph. The diversity introduced by wavelength range should help in disentangling static aberrations, residual turbulence structure function, coronagraph action, and the exoplanet faint flux. This focal-plane post-coronagraphic method has been pointed out by [32] as one of the most attractive, as it is directly sensitive to aberration perturbations in the focal plane. Note that as our coronagraphic image formation model is not accurate very close to the optical axis compared to a realistic coronagraphic mask, we can guess that wave-front sensing of low-order aberrations might be biased, as mentioned by [33].

5. CONCLUSION

We have developed and validated an analytical model for coronagraphic imaging through AO-corrected turbulence. This analytical model accounts for the major parameters of imaging through turbulence: the structure function of the residual turbulent phase, as well as upstream and downstream static aberrations. This analytical model can be used to compute and simulate long-exposure coronagraphic images very efficiently without the need for the computer-intensive simulation of numerous short exposures. It can also be used as a data model in inversion procedures such as image restoration or planet detection methods.

With realistic miscalibrations of φ_u and D_φ we have shown that subtracting the analytical model from the image brings roughly a factor of 10 attenuation in the residual coronagraphic image, which itself brings about the same attenuation w.r.t. the non-coronagraphic image.

The analytical model has been implemented in a first inversion method based on a Bayesian approach, where the star flux and the observed object are jointly estimated.

For a planet contrast of 2.10^4 and SPHERE conditions, this inversion method showed a SNR increase from a value of 3 in the raw image up to 30 in the image difference $\mathbf{i}_\Delta$, and up to 160 in the restoration.

Short-term future work includes the validation of this model on laboratory coronagraphic data. Work in progress not presented in this paper suggests that this model can be used as an essential build-in bloc of a coronagraphic phase diversity wavefront sensor.

Long-term future work includes the development of a global processing method allowing one to use this model image, e.g., in contexts such as angular differential imaging, dual band imaging, or IFS imaging. This global processing method will allow one to estimate observed object intensity as well as system parameters.

APPENDIX A: CONNECTION WITH OTHER DEFINITIONS OF PERFECT CORONAGRAPH

In order to establish the connection between our adopted definition of the perfect coronagraph [15,8], let us in this appendix briefly consider the case of a long exposure, and assume that:

- $\varphi_u(\rho,t)$ is considered a zero-mean random spatial field,
- $\varphi_r(\rho,t)$ and $\varphi_u(\rho,t)$ are ergodic with respect to space (i.e., there is an equivalence between expected value and spatial integration),

- the surface S of the pupil is wide enough to guarantee that spatial statistics on the aperture are well estimated,

then it is easy to show using Eqs. (1) and (6), that $\eta_0(t)$ defined as Eq. (5) does not depend on time and that one can identify the expected value $\langle|\eta_0(t)|^2\rangle$ with the coherent energy E_c, defined as

$$E_c = e^{-\sigma^2_{\varphi_r(\boldsymbol{\rho},t)+\varphi_u}}, \tag{A1}$$

with σ_f^2 being the spatial variance of function f in the pupil defined as

$$\sigma_f^2 = \frac{1}{S}\int\int_S \left(f^2(\boldsymbol{\rho}) - \left(\frac{1}{S}\int\int_S f(\boldsymbol{\rho}')\mathrm{d}^2\boldsymbol{\rho}'\right)\right)^2 \mathrm{d}^2\boldsymbol{\rho},$$

which does not depend on time with the above assumptions. In [15,8], the perfect coronagraph was defined as subtracting an Airy pattern weighted by $\sqrt{E_c}$. From the above we can see that such a definition is valid only in a long-exposure case with an ergodicity assumption and an infinite pupil size. On the other hand, the definition of Eq. (6), which is the instantaneous SR and is used in the paper, makes sense whatever the phase statistics may be.

ACKNOWLEDGMENTS

The authors want to thank Marie Ygouf for her careful proofreading of this paper, as well as the reviewers for their highly perceptive review. This work also received the support of PHASE, the high-angular-resolution partnership among ONERA, Observatoire de Paris, CNRS, and Université Paris Diderot.

REFERENCES

1. B. A. Macintosh, J. R. Graham, D. W. Palmer, R. Doyon, J. Dunn, D. T. Gavel, J. Larkin, B. Oppenheimer, L. Saddlemyer, A. Sivaramakrishnan, J. K. Wallace, B. Bauman, D. A. Erickson, C. Marois, L. A. Poyneer, and R. Soummer, "The Gemini Planet Imager: from science to design to construction," Proc. SPIE **7015**, 701518 (2008).
2. J.-L. Beuzit, M. Feldt, K. Dohlen, D. Mouillet, P. Puget, and F. Wildi, "SPHERE: a 'planet finder' instrument for the VLT," Proc. SPIE **7014**, 701418 (2008).
3. J. M. Conan, P. Y. Madec, and G. Rousset, "Evaluation of image quality obtained with adaptive optics partial correction," in *Progress in Telescope and Instrumentation Technologies*, ESO Conference and Workshop Proceedings, M.-H. Ulrich, ed. (ESO, 1992), p. 475.
4. J.-P. Véran, F. Rigaut, H. Maître, and D. Rouan, "Estimation of the adaptive optics long-exposure point-spread function using control loop data," J. Opt. Soc. Am. A **14**, 3057–3069 (1997).
5. E. E. Bloemhof, R. G. Dekany, M. Troy, and B. R. Oppenheimer, "Behavior of remnant speckles in an adaptively corrected imaging system," Astrophys. J. **558**, L71–L74 (2001).
6. A. Sivaramakrishnan, C. D. Koresko, R. B. Makidon, T. Berkefeld, and M. J. Kuchner, "Ground-based coronagraphy with high-order adaptive optics," Astrophys. J. **552**, 397–408 (2001).
7. M. D. Perrin, A. Sivaramakrishnan, R. B. Makidon, B. R. Oppenheimer, and J. R. Graham, "The structure of high Strehl ratio point-spread functions," Astrophys. J. **596**, 702–712 (2003).
8. C. Cavarroc, A. Boccaletti, P. Baudoz, T. Fusco, and D. Rouan, "Fundamental limitations on Earth-like planet detection with extremely large telescopes," Astron. Astrophys. **447**, 397–403 (2006).
9. C. Marois, D. Lafrenière, R. Doyon, B. Macintosh, and D. Nadeau, "Angular differential imaging: A powerful high-contrast imaging technique," Astrophys. J. **641**, 556–564 (2006).
10. D. Lafrenière, C. Marois, R. Doyon, D. Nadeau, and É. Artigau, "A new algorithm for point-spread function subtraction in high-contrast imaging: A demonstration with angular differential imaging," Astrophys. J. **660**, 770–780 (2007).
11. L. M. Mugnier, A. Cornia, J.-F. Sauvage, G. Rousset, T. Fusco, and N. Védrenne, "Optimal method for exoplanet detection by angular differential imaging," J. Opt. Soc. Am. A **26**, 1326–1334 (2009).
12. C. Marois, R. Doyon, D. Nadeau, R. Racine, M. Riopel, P. Vallée, and D. Lafrenière, "TRIDENT: an infrared differential imaging camera optimized for the detection of methanated substellar companions," Publ. Astron. Soc. Pac. **117**, 745–756 (2005).
13. A. Boccaletti, D. Mouillet, T. Fusco, P. Baudoz, C. Cavarroc, J.-L. Beuzit, C. Moutou, and K. Dohlen, "Analysis of ground-based differential imager performance," presented at IAUC 200, Direct Imaging of Exoplanets: Science and Techniques," Nice, France, October 2005 (2005).
14. I. Smith, M. Carbillet, A. Ferrari, D. Mouillet, A. Boccaletti, and K. Dohlen, "Simulation of moving exoplanets detection using the VLT instrument SPHERE/IRDIS," Proc. SPIE **7015**, 70156F (2008).
15. C. Aime and R. Soummer, "The usefulness and limits of coronagraphy in the presence of pinned speckles," Astrophys. J. Lett. **612**, L85–L88 (2004).
16. R. Soummer, K. Dohlen, and C. Aime, "Achromatic dual-zone phase mask stellar coronagraph," Astron. Astrophys. **403**, 369–381 (2003).
17. M. Born and E. Wolf, *Principles of Optics*, 6th (corrected) ed. (Pergamon Press, 1993).
18. F. Roddier, "The effects of atmospherical turbulence in optical astronomy," in *Progress in Optics*, Vol. XIX, E. Wolf, ed. (North Holland, 1981), pp. 281–376.
19. T. Fusco, G. Rousset, J.-F. Sauvage, C. Petit, J.-L. Beuzit, K. Dohlen, D. Mouillet, J. Charton, M. Nicolle, M. Kasper, and P. Puget, "High order adaptive optics requirements for direct detection of extra-solar planets. application to the sphere instrument," Opt. Express **14**, 7515–7534 (2006).
20. L. Jolissaint, J.-P. Véran, and R. Conan, "Analytical modeling of adaptive optics: foundations of the phase spatial power spectrum approach," J. Opt. Soc. Am. A **23**, 382–394 (2006).
21. L. A. Poyneer and B. Macintosh, "Spatially filtered wavefront sensor for high-order adaptive optics," J. Opt. Soc. Am. A **21**, 810–819 (2004).
22. T. Fusco, C. Petit, G. Rousset, J.-M. Conan, and J.-L. Beuzit, "Closed-loop experimental validation of the spatially filtered Shack–Hartmann concept," Opt. Lett. **30**, 1255–1257 (2005).
23. J.-F. Sauvage, T. Fusco, G. Rousset, and C. Petit, "Calibration and pre-compensation of non-common path aberrations for extreme adaptive optics," J. Opt. Soc. Am. A **24**, 2334–2346 (2007).
24. D. Rouan, P. Riaud, A. Boccaletti, Y. Clénet, and A. Labeyrie, "The four-quadrant phase-mask coronagraph. I. Principle," Publ. Astron. Soc. Pac. **112**, 1479–1486 (2000).
25. F. Malbet, "High angular resolution coronography for adaptive optics," Astron. Astrophys. Suppl. Ser. **115**, 161–174 (1996).
26. R. Racine, G. A. Walker, D. Nadeau, and C. Marois, "Speckle noise and the detection of faint companions'," Publ. Astron. Soc. Pac. **112**, 587 (1999).
27. J.-M. Conan, L. M. Mugnier, T. Fusco, V. Michau, and G. Rousset, "Myopic deconvolution of adaptive optics images by use of object and point spread function power spectra," Appl. Opt. **37**, 4614–4622 (1998).
28. L. M. Mugnier, T. Fusco, and J.-M. Conan, "MISTRAL: a myopic edge-preserving image restoration method with application to astronomical adaptive-optics-corrected long-

exposure images," J. Opt. Soc. Am. A **21**, 1841–1854 (2004).
29. D. Gratadour, D. Rouan, L. M. Mugnier, T. Fusco, Y. Clénet, E. Gendron, and F. Lacombe, "Near-IR AO dissection of the core of NGC 1068 with NaCo," Astron. Astrophys. **446**, 813–825 (2006).
30. T. Fusco, G. Rousset, D. Rabaud, E. Gendron, D. Mouillet, F. Lacombe, G. Zins, P.-Y. Madec, A.-M. Lagrange, J. Charton, D. Rouan, H. Hubin, and N. Ageorges, "NAOS on-line characterization of turbulence parameters and adaptive optics performance," J. Opt. A, Pure Appl. Opt. **6**, 585–596 (2004).
31. J.-F. Sauvage, L. Mugnier, T. Fusco, and G. Rousset, "Post processing of differential images for direct extrasolar planet detection from the ground," Proc. SPIE **6272**, 62722B (2006).
32. J. K. Wallace, J. J. Green, M. Shao, M. Troy, J. P. Lloyd, and B. Macintosh, "Science camera calibration for extreme adaptive optics," Proc. SPIE **5490**, 370–378 (2004).
33. A. Sivaramakrishnan, R. Soummer, L. Pueyo, J. K. Wallace, and M. Shao, "Sensing phase aberrations behind Lyot coronagraphs," Astrophys. J. **688**, 701–708 (2008).